Electronic Supplementary Information

Experiment Section

Materials: $NiCl_2\cdot 6H_2O$, hexamethylene tetramine (HMT), $CoCl_2\cdot 6H_2O$, NH_4F, $CO(NH_2)_2$, $FeCl_3\cdot 6H_2O$, Na_2SO_4 and carbon paper (CP) were bought from Beijing Chemical Corporation. Ethanol (C_2H_5OH), hydrochloric acid (HCl), sodium hydroxide (NaOH, 99.0%), ammonium chloride (NH_4Cl), sodium salicylate ($C_7H_5O_3Na$), *p*-dimethylaminobenzaldehyde ($C_9H_{11}NO$), sodium nitroferricyanide dihydrate ($C_5FeN_6Na_2O\cdot 2H_2O$), sodium hypochlorite solution (NaClO), sodium nitrate ($NaNO_3$), sulfamic acid and sodium hypophosphite (NaH_2PO_2) was purchased from Aladdin Ltd. (Shanghai, China). The water use throughout all experiments was purified through a Millipore system. All chemicals were used of analytical grade and used as received without further purification.

Synthesis of $Ni(OH)_2$/CP precursor: CP was pretreated in 0.05 M H_2SO_4 and sequentially cleaned in C_2H_5OH and deionized water. The cleaned CP was immersed into a 40 mL aqueous solution containing 5 mmol $NiCl_2\cdot 6H_2O$ and 10 mmol HMT at room temperature. The aqueous solution with the CP were transferred to a 50 mL Teflon-lined stainless-steel autoclave and maintained at 100 °C for 10 h, and then allowed to cool down. The CP with precursor was washed with water several times and dried in oven.

Synthesis of Ni_2P/CP: $Ni(OH)_2$/CP and NaH_2PO_2 were placed at two separate positions in one closed porcelain crucible with NaH_2PO_2 at the upstream side of the furnace. Subsequently, the samples were heated at 280 °C for 2 h with a heating speed of 1 $°C\ min^{-1}$ in Ar atmosphere. Ni_2P/CP was collected after cooled to ambient temperature under Ar.

Synthesis of CoP/CP: The cleaned CP was immersed into a 35 mL aqueous solution containing 0.397 g $CoCl_2\cdot 6H_2O$, 0.155 g NH_4F, and 0.500 g $CO(NH_2)_2$ at room temperature. The aqueous solution with the CP were transferred to a 50 mL Teflon-lined stainless-steel autoclave and maintained at 120 °C for 6 h, and then allowed to cool down. The as-fabricated Co(OH)F /CP was cleaned with water and air dried then. After that, it was placed in a tube furnace with another 1 g of NaH_2PO_2 at the upstream position. With only 2 h of heating treatment at 300 °C with a heating speed of 2 °C min^{-1} under Ar atmosphere, the self-supported CoP/CP can be obtained.

Synthesis of FeP/CP: The cleaned CP was immersed into a 35 mL aqueous solution containing 0.4 g $FeCl_3 \cdot 6H_2O$ and 0.24 g Na_2SO_4 at room temperature. The aqueous solution with the CP were transferred to a 50 mL Teflon-lined stainless-steel autoclave and maintained at 120 °C for 6 h, and then allowed to cool down. The as-fabricated Fe_2O_3/CP was obtained after annealing in Ar gas at 450 °C for 3 h. Fe_2O_3/CP and NaH_2PO_2 were placed at two separate positions in one closed porcelain crucible with NaH_2PO_2 at the upstream side of the furnace. Subsequently, the samples were heated at 300 °C for 2 h with a heating speed of 2 °C min^{-1} in Ar atmosphere. After that, FeP/CP was collected after cooled to ambient temperature under Ar atmosphere.

Characterization: XRD data were acquired on a Shimadzu XRD-6100 diffractometer with Cu Kα radiation (40 kV, 30 mA) of wavelength 0.154 nm. SEM and EDX elemental mapping images were collected on a Gemini SEM 300 scanning electron microscope (ZEISS, Germany) at an accelerating voltage of 5 kV. XPS measurements were performed on an ESCALABMK II X-ray photoelectron spectrometer using Mg as the exciting source. TEM images were obtained from a Zeiss Libra 200FE transmission electron microscope operated at 200 kV. Absorbance data were acquired on SHIMADZU UV-2700 UV-Vis spectrophotometer. Gas chromatography analysis was performed on GC-2014C (Shimadzu Co.) with thermal conductivity detector and nitrogen carrier gas.

Electrochemical measurements: Electrochemical measurements were performed in a two-compartment cell separated by a treated Nafion 117 membrane using a CHI 660E electrochemical analyzer (CHI Instruments, Inc.). The electrochemical experiments were carried out with a three-electrode configuration using Ni_2P/CP with a cutting size of 0.25 cm^2 as working electrodes, a platinum foil (4 cm^2) as the counter electrode, and a standard Ag/AgCl reference electrode. In all measurements, saturated Ag/AgCl electrode was calibrated to RHE if there are no special notes as following: E (RHE) = E (Ag/AgCl) + 0.059 × pH + 0.197 V. LSV was conducted at a scan rate of 5 mV s^{-1} with iR correction. Before each measurement, NO or Ar was purged into the solution for at least 30 min to remove residual air in the reservoir. Controlled potential electrolysis was then performed at each potential for 1 h. ECSA was measured by CV at the potential window from −0.3 to −0.2 V versus Ag/AgCl, with different scan rates of 20, 30, 40, 50, 60, 70, 80, 90 and 100 mV s^{-1}. The double-layer capacitance (C_{dl}) was estimated by plotting the $\Delta j = (j_a - j_c)$ at −0.25 V versus Ag/AgCl against the scan rates, in which the j_a and j_c were the anodic and cathodic current density, respectively. The slope is twice that of the C_{dl} values. C_{dl} was used to represent the ECSA. All the above measurements were at room temperature under atmospheric pressure and carried out without ohmic-drop correction unless noted otherwise. The area of the working electrode in the electrolyte was controlled at 0.25 cm^2, and all current densities were normalized to the geometrical area of the electrode.

Determination of NH_3: The amount of NH_3 in the solution was determined by colorimetry using the indophenol blue method.[1] A certain amount of electrolyte was taken out from the electrolytic cell and diluted to 2 mL to the detection range. Then, 2 mL of 1 M NaOH solution that contains salicylic acid and sodium citrate was added. Then, 1 mL of 0.05 M NaClO and 0.2 mL of 1 wt% $C_5FeN_6Na_2O\cdot 2H_2O$ were added to the above solution. After standing at room temperature for 2 h, the UV-Vis absorption spectrum was measured. The concentration of NH_3 was determined using the absorbance at a wavelength of 660 nm. The concentration-absorbance curve was calibrated using a series of standard NH_4Cl solutions.

Determination of N_2H_4: The N_2H_4 presented in the electrolyte was estimated by Watt and Chrisp method.[2] Color reagent includes $C_9H_{11}NO$ (5.99 g), HCl (concentrated, 30 mL) and ethanol (300 mL). 1 mL above color reagent and 1 mL electrolyte were mixed and stirred 15 min at room temperature. The concentration of N_2H_4 was determined using the absorbance at a wavelength of 455 nm. The absorbance curves were calibrated using standard N_2H_4 solution with a series of concentrations.

Determination of NO_3^-: Firstly, a certain amount of electrolyte was taken out from the electrolytic cell and diluted to 5 mL to the detection range. Then, 0.1 mL 1 M HCl and 0.01 mL 0.8 wt% sulfamic acid solution were added into the aforementioned solution. The absorption spectrum was measured using a UV-Vis spectrophotometer and the absorption intensities at a wavelength of 220 nm and 275 nm were recorded. The final absorbance value was calculated by this equation: $A = A_{220nm} - 2A_{275nm}$. The concentration-absorbance curve was calibrated using a series of standard $NaNO_3$ solutions and the $NaNO_3$ crystal was dried at 105–110 °C for 2 h in advance.

Determination of H_2: The gas product (H_2) was monitored by GC.

Determination of FE and NH_3 yield: The FE for NH_3 electrosynthesis was defined as the amount of electric charge used for producing NH_3 divided by the total charge passed through the electrodes during the electrolysis. The FE was calculated according to the following equation:

$$FE = n \times F \times c \times V / (M \times Q) \quad (1)$$

The NH_3 yield was calculated using the following equation:

$$NH_3 \text{ yield} = c_{NH3} \times V / (17 \times t \times S) \quad (2)$$

Where n is the number of electrons was needed to produce one product molecule, F is Faraday constant (96485 C mol^{-1}); c is the measured mass concentration of product; V is the volume of the cathodic reaction electrolyte (50 mL); M is relative molecular mass of specific product; Q is the quantity of applied charge/electricity; t is the time for which the potential was applied (1 h); S is the geometric area of the working electrode (0.25 cm^2).

Zn–NO battery: Ni_2P/CP was employed as the cathode to perform the NORR in a cathodic electrolyte (0.1 M HCl). A polished Zn plate was set in an anodic electrolyte (1 M KOH), and a bipolar membrane was used to separate the two different electrolytes. During the battery discharge process, electrochemical NO reduction occurs on Ni_2P/CP, and Zn converts to ZnO. The electrochemical reactions on each electrode can be described as follows:

$$\text{Cathode: } NO + 5H^+ + 5e^- \rightarrow NH_3 + H_2O \quad (3)$$

Anode: $Zn + 2OH^{-} \rightarrow ZnO + H_2O + 2e^{-}$ (4)

Overall: $5Zn + 2NO + 3H_2O \rightarrow 5ZnO + 2NH_3$ (5)

As displayed in Table S4, Zn-NO battery potentially has a higher voltage output than those of metal-air batteries, metal-CO_2 batteries, etc. The NH_3 yield is quantified by using colorimetric methods. Power density is calculated using equation (P=UI) from the results of polarization data (Table S5).

Computational details: Spin-polarized first-principles calculations were performed with Vienna ab initio simulation package (VASP) within the framework of density functional theory (DFT).[3] Perdew, Burke, and Ernzerhof (PBE) functional[4] and Projected augment wave (PAW) pseudopotential[5] were adopted to treat the exchange-correlation effect and the interaction between the valence electrons with ionic cores, respectively. The long-range dispersion interaction was described by the DFT-D3 method.[6] The convergence criteria for the total energy and the Hellman-Feynman force are 10^{-4} eV and 0.03 eVÅ^{-1}, respectively. To simulate the reaction on the Ni_2P (111) surface, the (1×2) supercell was used with a vacuum layer of ~ 18 Å, for which the first Brillouin zone was sampled via Monkhorst-Pack (MP) grid[7] of 3×2×1 with the cutoff energy for the plane-wave basis of 450 eV. The charge transfer was calculated using Bader analysis.[8]

The computational hydrogen electrode (CHE) model has been used to study the change in Gibbs free energy for the elemental steps,[9] using the following equation:

$$\Delta G = \Delta E + \Delta E_{\mathrm{ZPE}} - T\Delta S \quad (6)$$

Here, E, E_{ZPE}, S, and T denote the DFT total energy, zero-point energy, entropy, and absolute temperature (298.15 K), respectively. Zero-point energy and entropy of the intermediates were obtained from DFT calculations (as displayed in Table S3), while the corrections of the free molecules taken from the NIST databases.[10]

The Ni_2P (111) surface can expose different terminations, and to determine the most stable one, we calculated and compared the surface energy (γ) of the various terminations according to the equation:

$$\gamma = \frac{1}{2A}\left[E_{slab}^{unrelax} - nE_{bulk}\right] + \frac{1}{A}\left[E_{slab}^{relax} - E_{slab}^{unrelax}\right] \quad (7)$$

where, A is the surface aera of one side of the slab; n is the number of Ni_2P units of the slab; E_{bulk} is the total energy of the bulk Ni_2P formula unit; E_{slab}^{relax} and $E_{slab}^{unrelax}$ are the total energies of the relaxed and unrelaxed slabs, respectively.

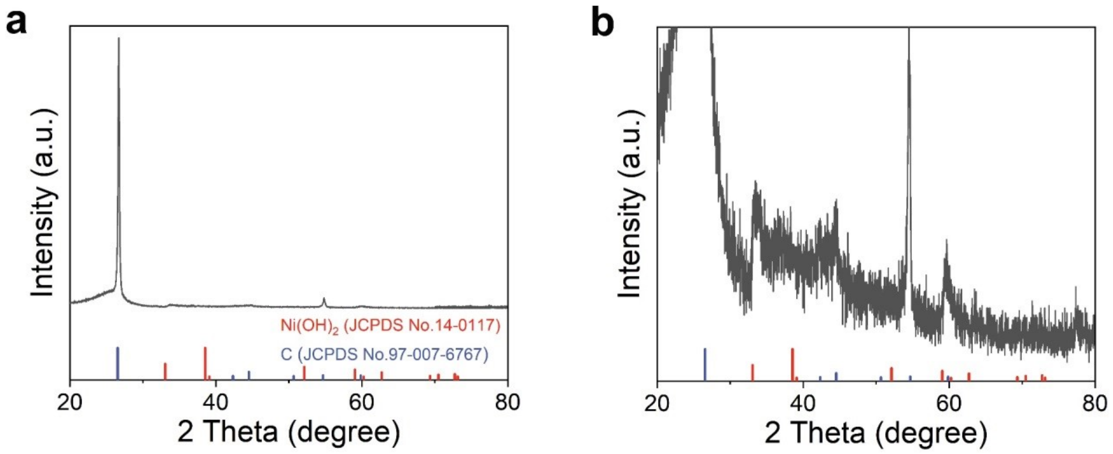

Fig. S1. XRD patterns of $Ni(OH)_2$/CP.

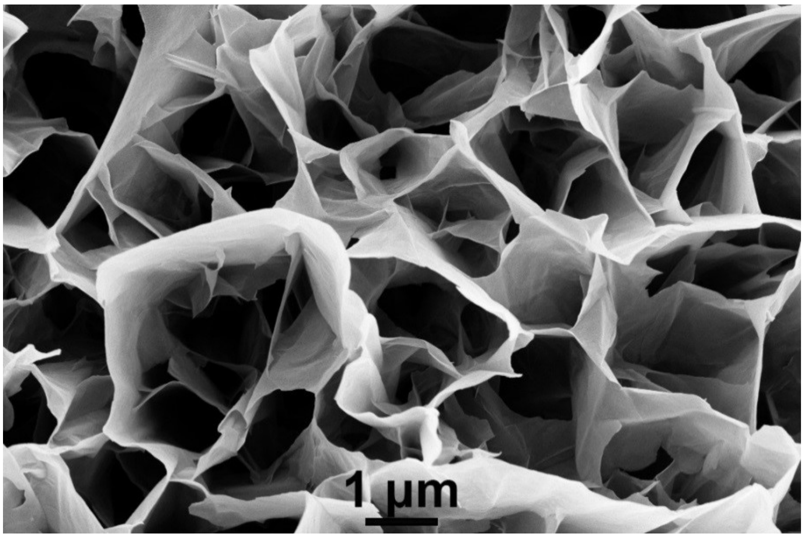

Fig. S2. SEM image of $Ni(OH)_2$/CP.

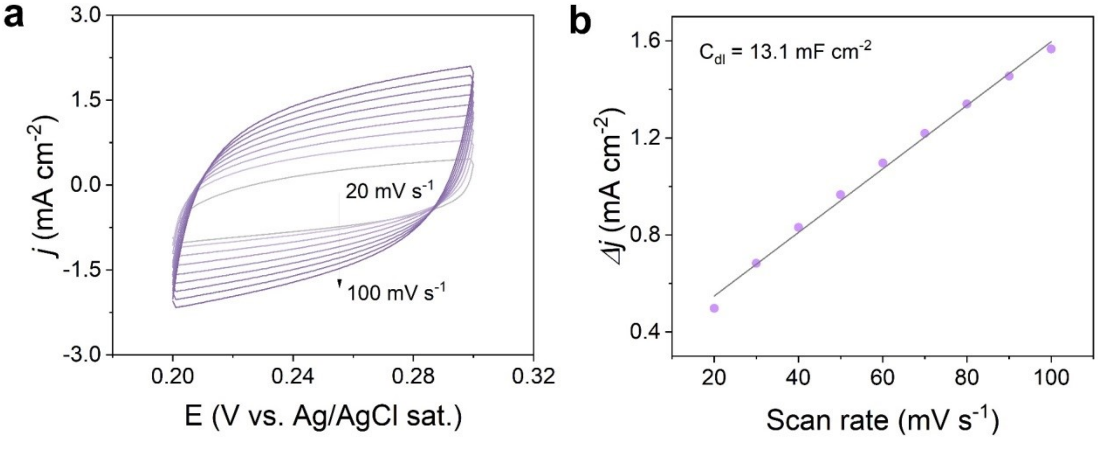

Fig. S3. (a) Cyclic voltammograms for Ni_2P/CP in the double layer region at different scan rates of 20, 30, 40, 50, 60, 70, 80, 90, and 100 mV s^{-1} in 0.1 M HCl electrolyte. (b) Capacitive current densities as a function of scan rates for Ni_2P/CP.

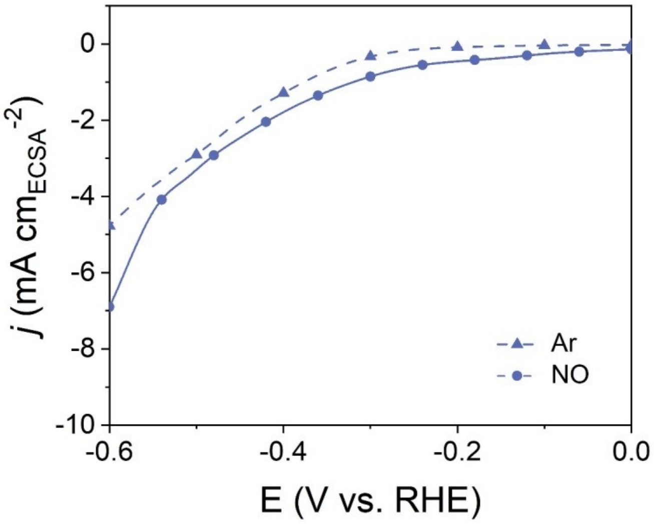

Fig. S4. ECSA-normalized LSV curves for Ni_2P/CP in Ar- and NO-saturated 0.1 M HCl.

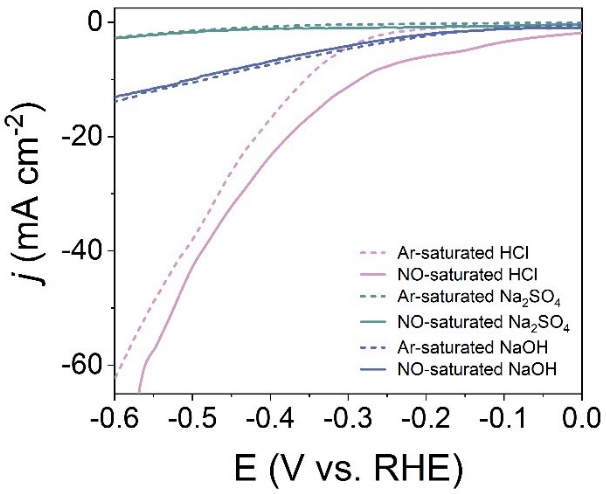

Fig. S5. Comparison of NORR activity of Ni_2P/CP in different electrolytes.

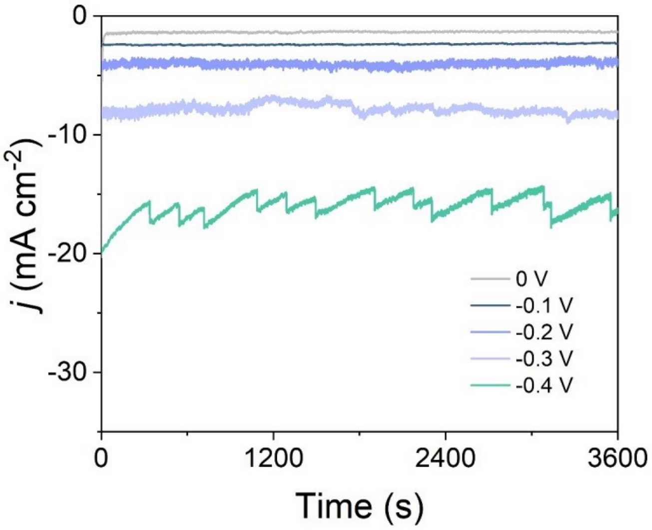

Fig. S6. CA curves at various applied potentials in NO-saturated 0.1 M HCl for Ni_2P/CP.

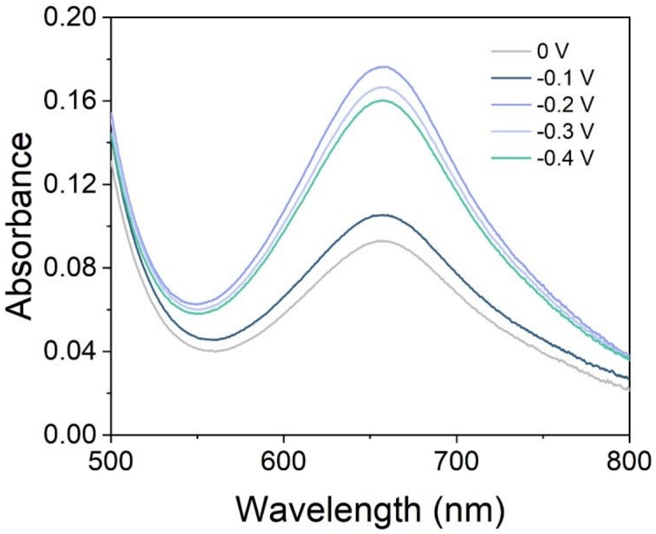

Fig. S7. UV-Vis absorption spectra of the electrolytes stained with indophenol indicator after 1 h electrolysis on Ni_2P/CP at various applied potentials.

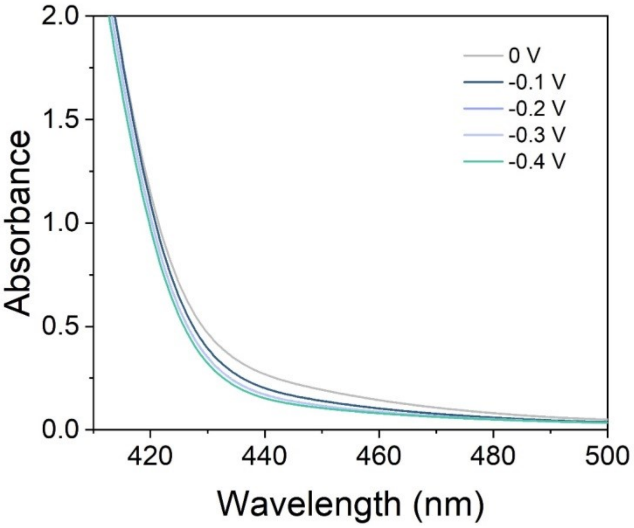

Fig. S8. UV-Vis absorption spectra of electrolytes estimated by the method of Watt and Chrisp after 1 h electrolysis on Ni_2P/CP at each given potential.

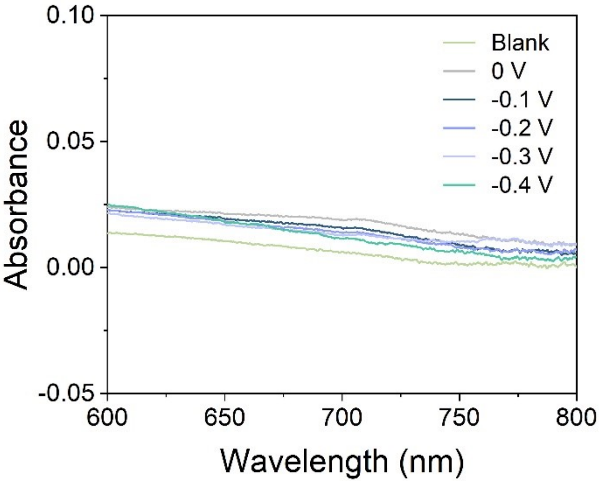

Fig. S9. UV-Vis absorption spectra for NH_2OH after 1 h electrolysis on Ni_2P/CP at each given potential.

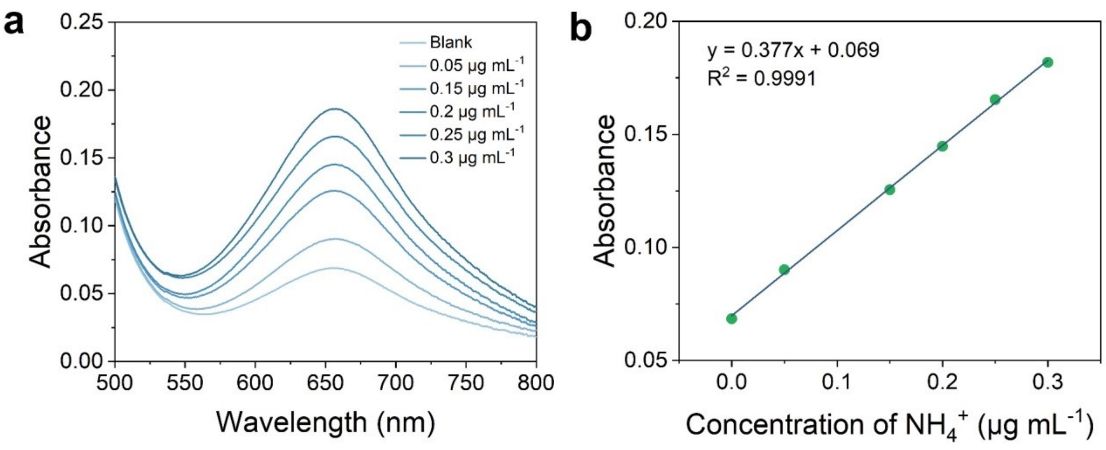

Fig. S10. (a) UV-Vis absorption spectra of indophenol assays with NH_3 after incubated for 2 h at room temperature and corresponding (b) calibration curve used for estimating NH_3.

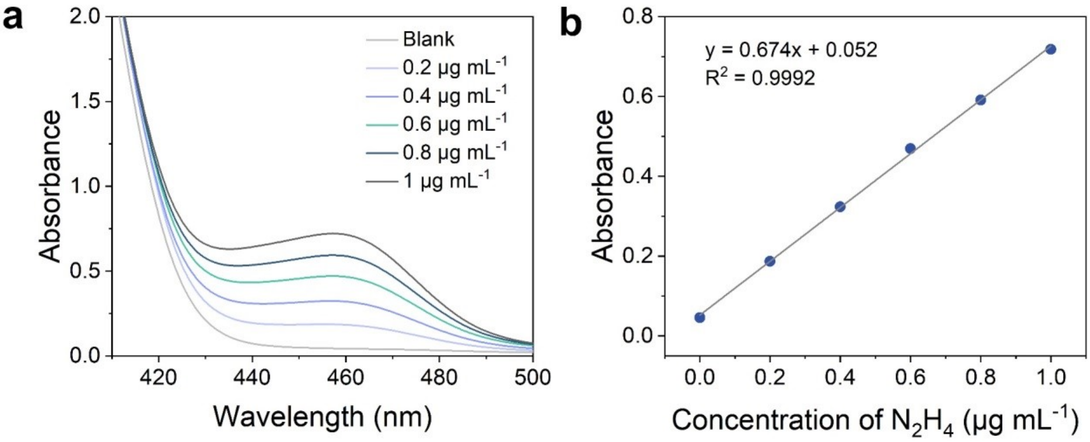

Fig. S11. (a) UV-Vis absorption spectra of various N_2H_4 concentration after incubated for 15 min at room temperature and corresponding (b) calibration curve used for estimating N_2H_4.

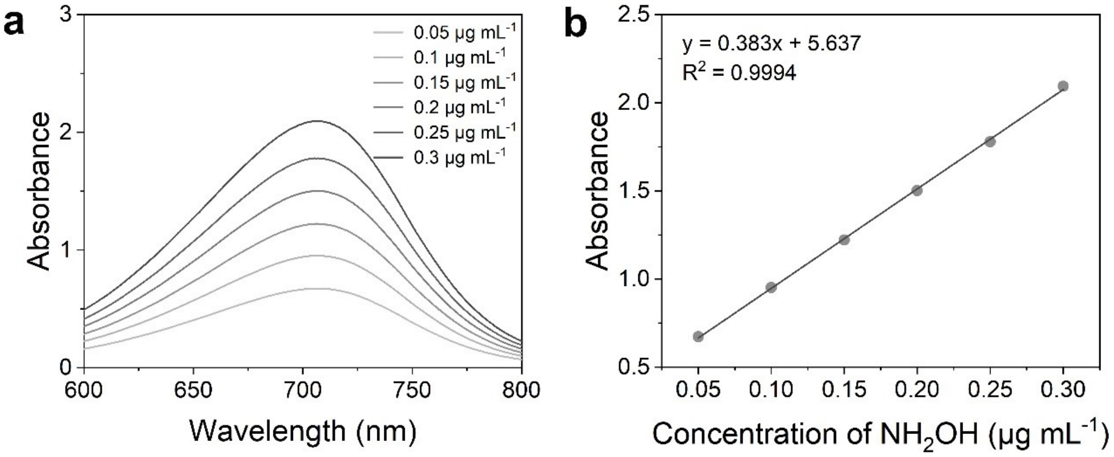

Fig. S12. (a) UV-Vis absorption spectra of various NH_2OH concentration after incubated for 1 min at 100 ℃ and corresponding (b) calibration curve used for estimating NH_2OH.

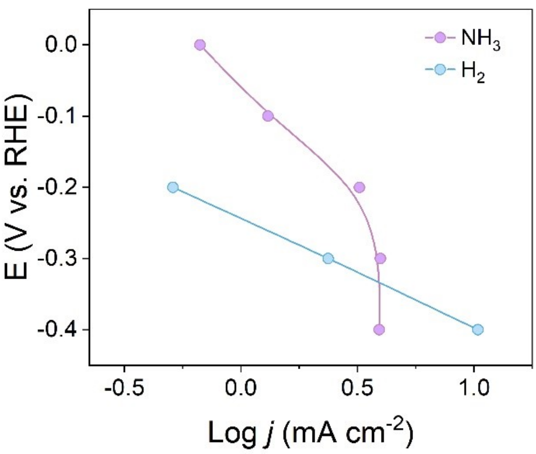

Fig. S13. Tafel plots obtained by multiplying the FEs for NH_3 and H_2 by the average current density at each potential.

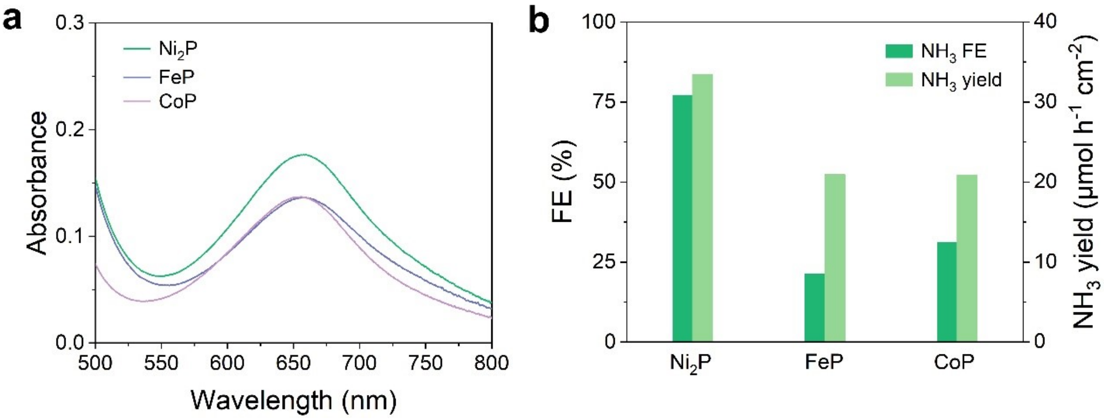

Fig. S14. (a) UV-Vis absorption spectra of the electrolytes stained with indophenol indicator after 1 h electrolysis on Ni_2P/CP, FeP/CP, and CoP/CP at –0.2 V. (b) Corresponding FEs and yields of NH_3 for Ni_2P/CP, FeP/CP, and CoP/CP at –0.2 V.

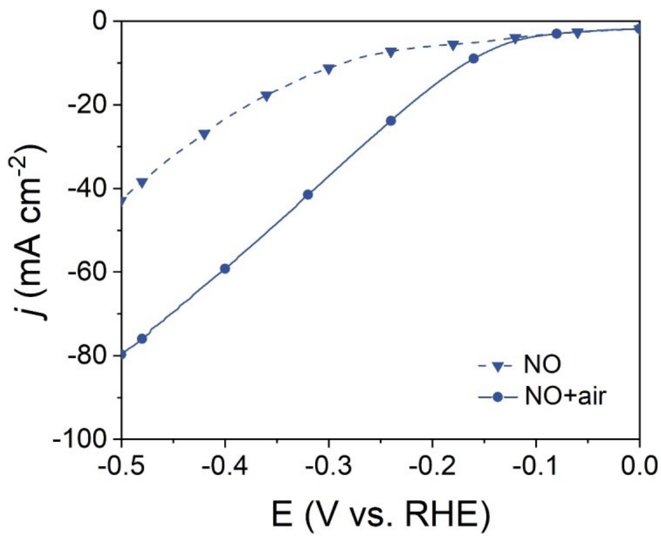

Fig. S15. LSV curves of Ni_2P/CP in the gas-tight (in NO-saturated electrolyte) and open electrolytic cells (under NO + air atmosphere).

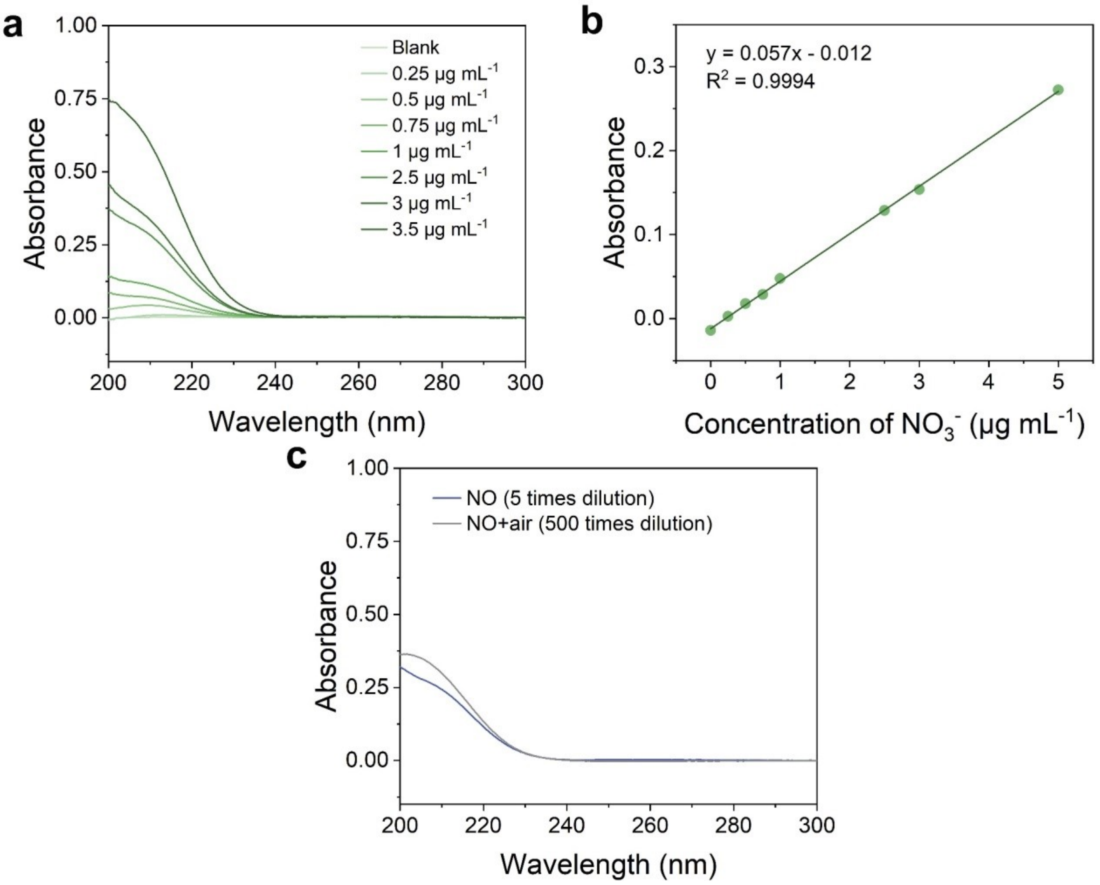

Fig. S16. (a) UV-Vis absorption spectra of various NO_3^- concentration after incubated for 20 min at room temperature and corresponding (b) calibration curve used for estimating NO_3^-. (c) UV-Vis absorption spectra of NO_3^- for Ni_2P/CP in a gas-tight (in NO-saturated electrolyte) and open chambers (under NO + air atmosphere) at −0.2 V after 1 h electrolysis.

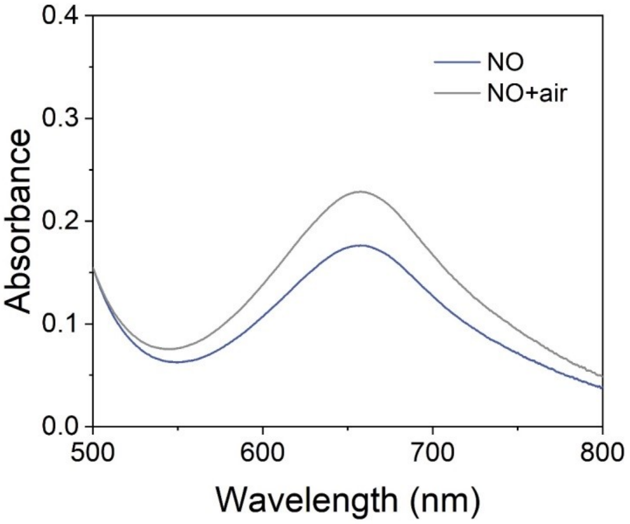

Fig. S17. UV-Vis absorption spectra of the electrolytes stained with indophenol indicator after 1 h electrolysis for Ni_2P/CP in a gas-tight and open cathodic chambers at −0.2 V.

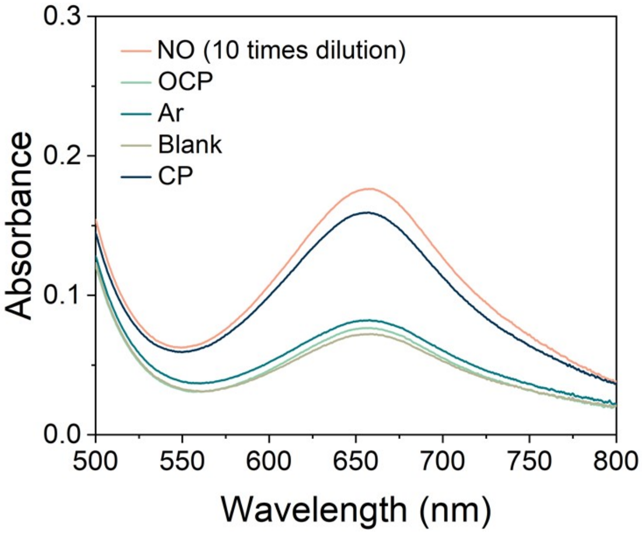

Fig. S18. UV-Vis absorption spectra of the electrolytes stained with indophenol indicator at different operating conditions.

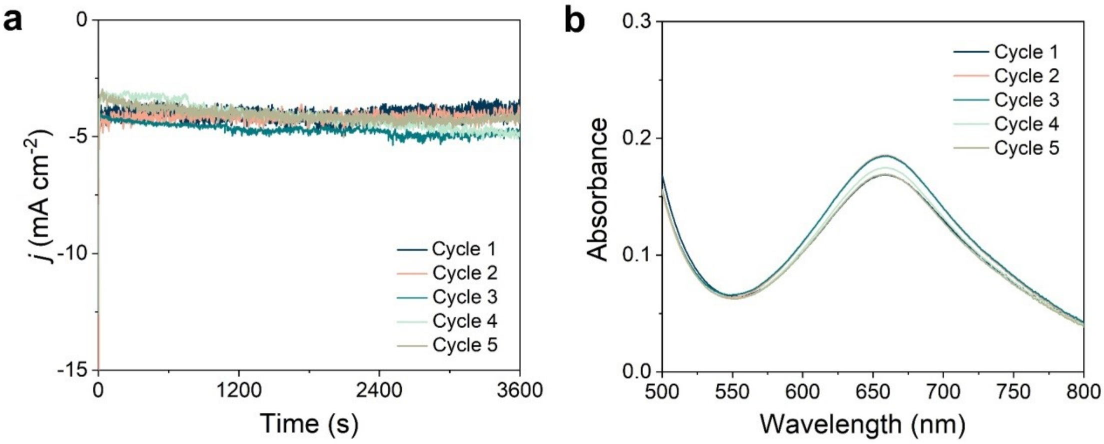

Fig. S19. (a) CA curves of recycling tests at −0.2 V in NO-saturated 0.1 M HCl for Ni_2P/CP. (b) UV-Vis absorption spectra of the electrolytes stained with indophenol indicator after recycling tests for NORR at –0.2 V in 0.1 M HCl.

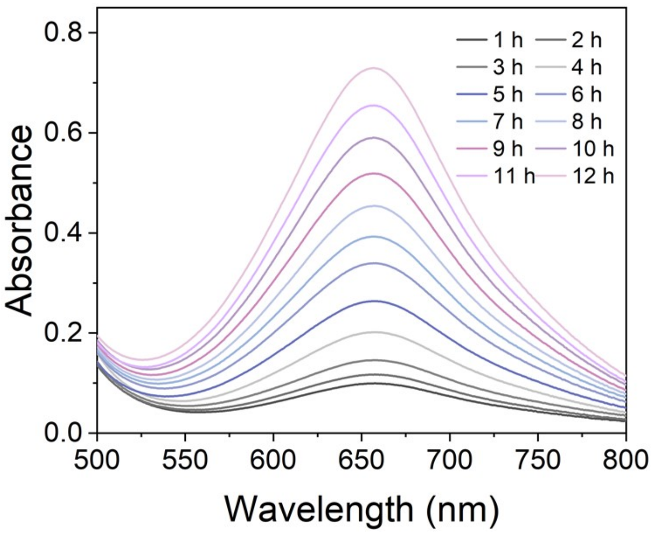

Fig. S20. UV-Vis absorption spectra of the electrolytes stained with indophenol indicator after 12 h electrolysis on Ni_2P/CP at –0.2 V.

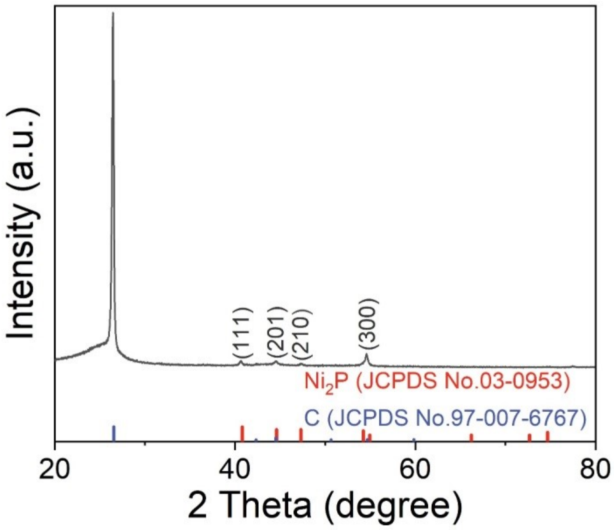

Fig. S21. XRD pattern of post-electrolysis Ni_2P/CP.

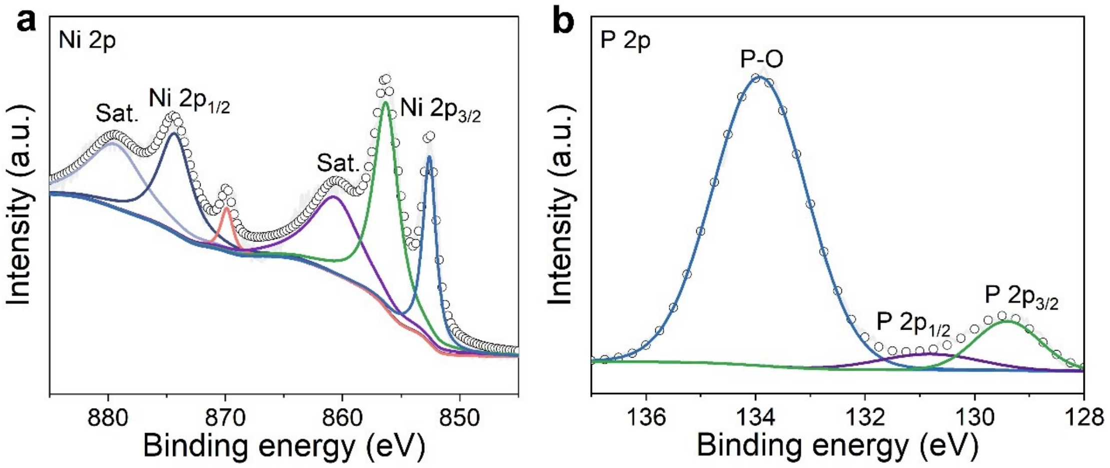

Fig. S22. XPS spectra of Ni_2P in (a) Ni 2p and (b) P 2p regions after stability test.

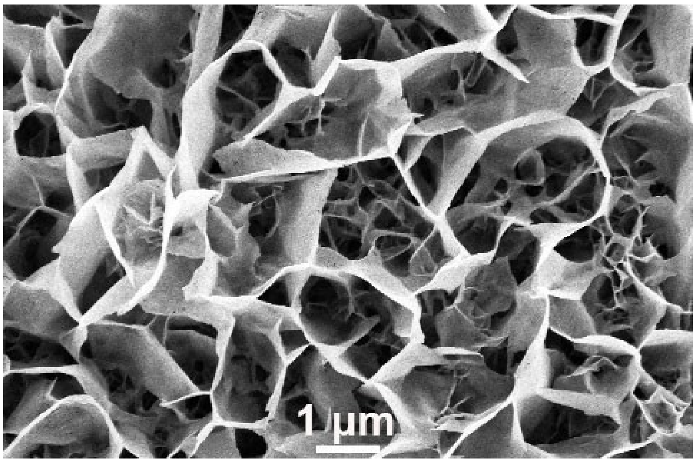

Fig. S23. SEM image of post-electrolysis Ni_2P/CP.

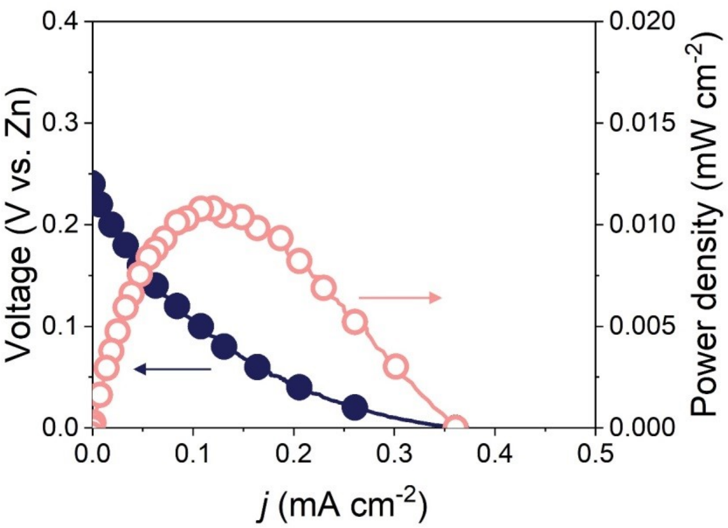

Fig. S24. Polarization and power density plots of CP-based Zn–NO battery.

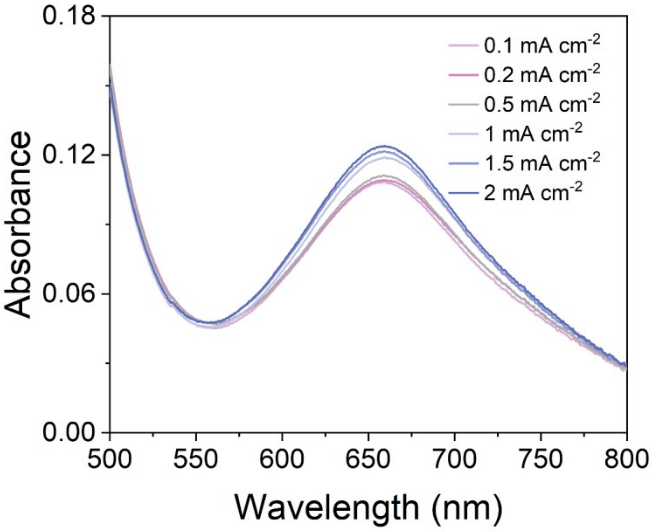

Fig. S25. UV-Vis absorption spectra of the electrolytes stained with indophenol indicator at different discharging current densities per 1800s of Ni_2P/CP-based Zn–NO battery.

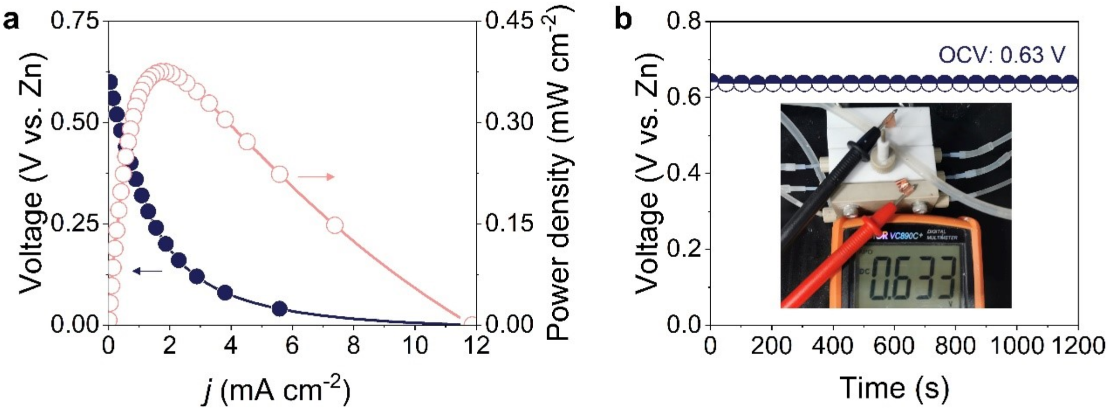

Fig. S26. (a) Polarization and power density plots of the assembled Zn–NO battery with the Ni_2P/CP cathode (using 1.0 M KOH solution as both anolyte and catholyte). (b) Corresponding OCV of the assembled Zn–NO battery.

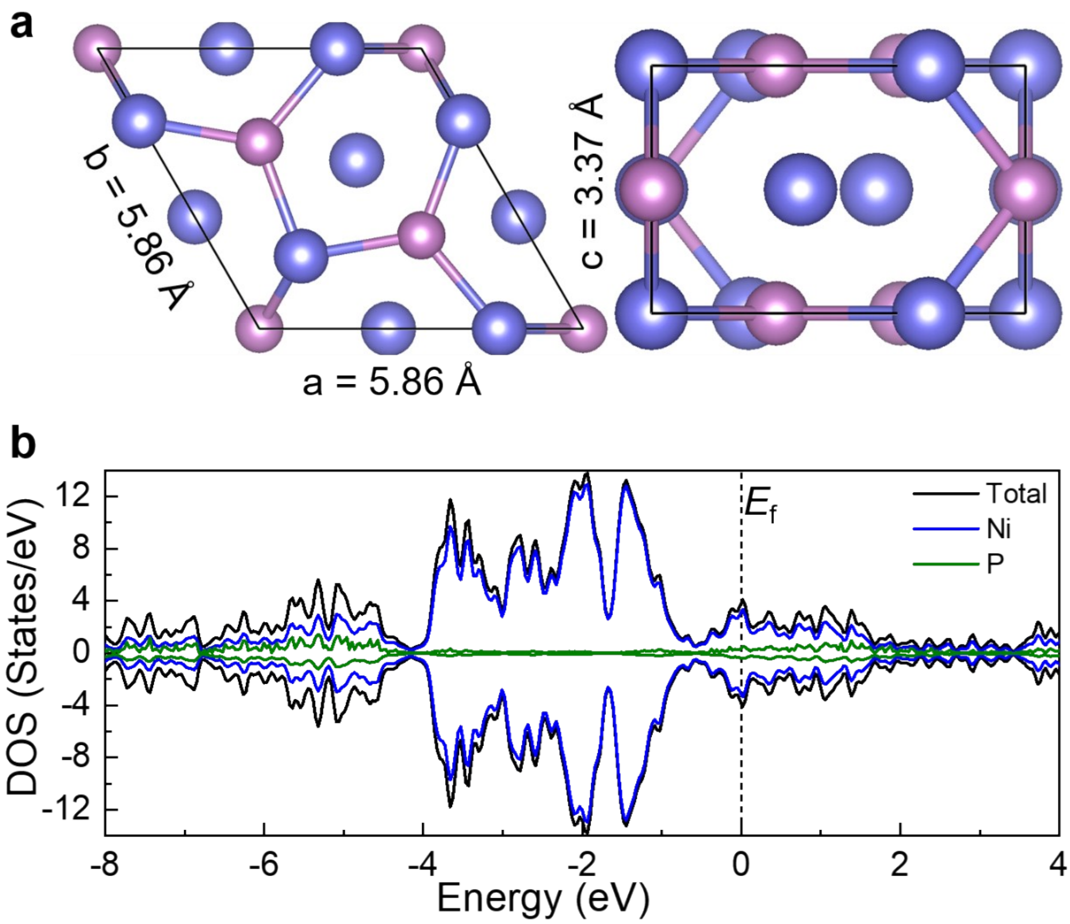

Fig. S27. (a) Unit cell together with the lattice parameters and (b) the calculated total densities of states of the Ni_2P bulk and the local densities of states of the Ni and P atoms. The dashed line in (b) denotes the position of the Fermi level (E_f). light blue and pink spheres represent Ni and P atoms, respectively.

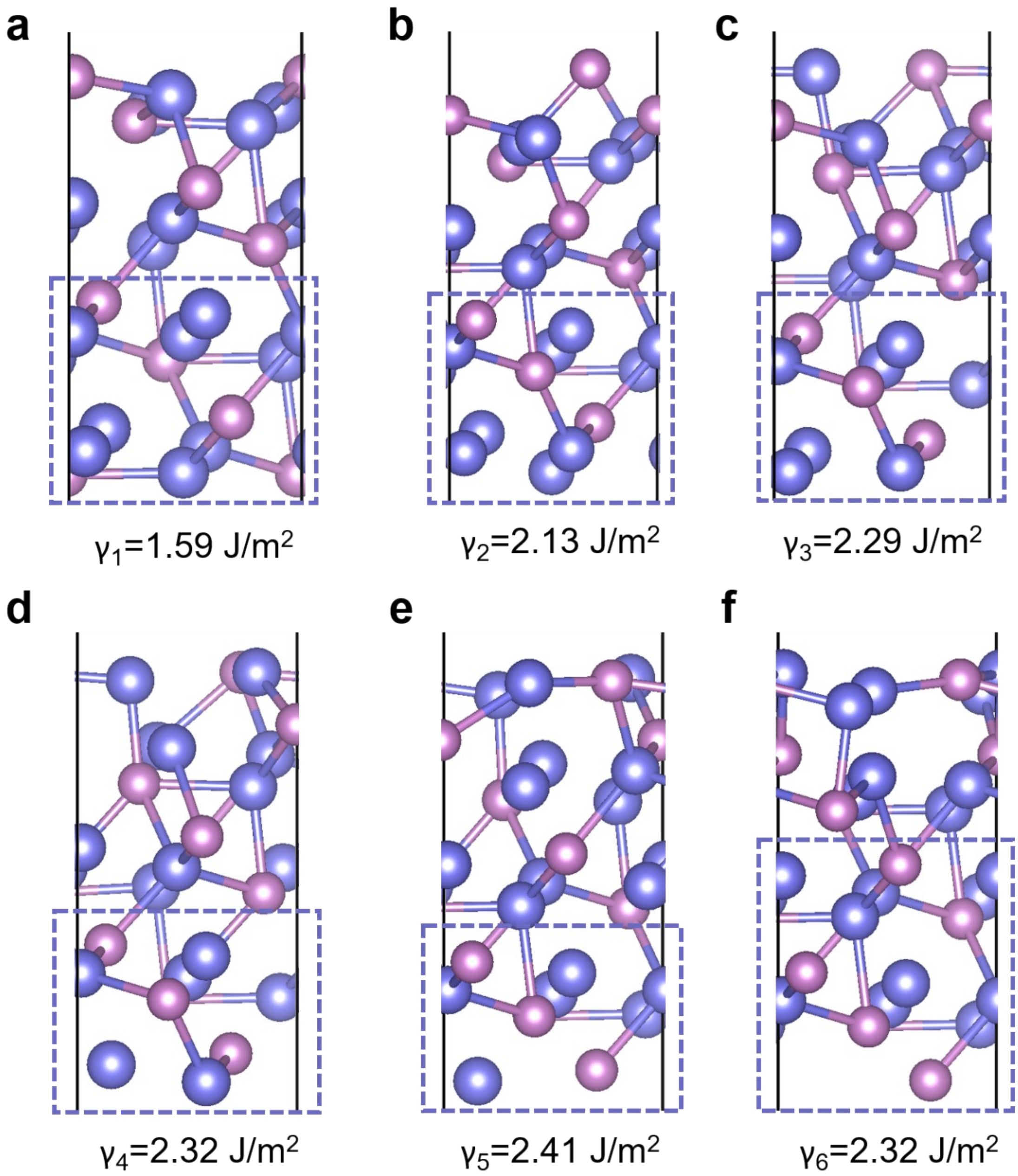

Fig. S28. Side views of the stab models of the Ni_2P (111) (1×1) surface with six different terminations. The atomic layers in the unit cell enclosed by the dashed bule lines are fixed to mimic the bulk. The surface energies (γ) for the six surfaces are given.

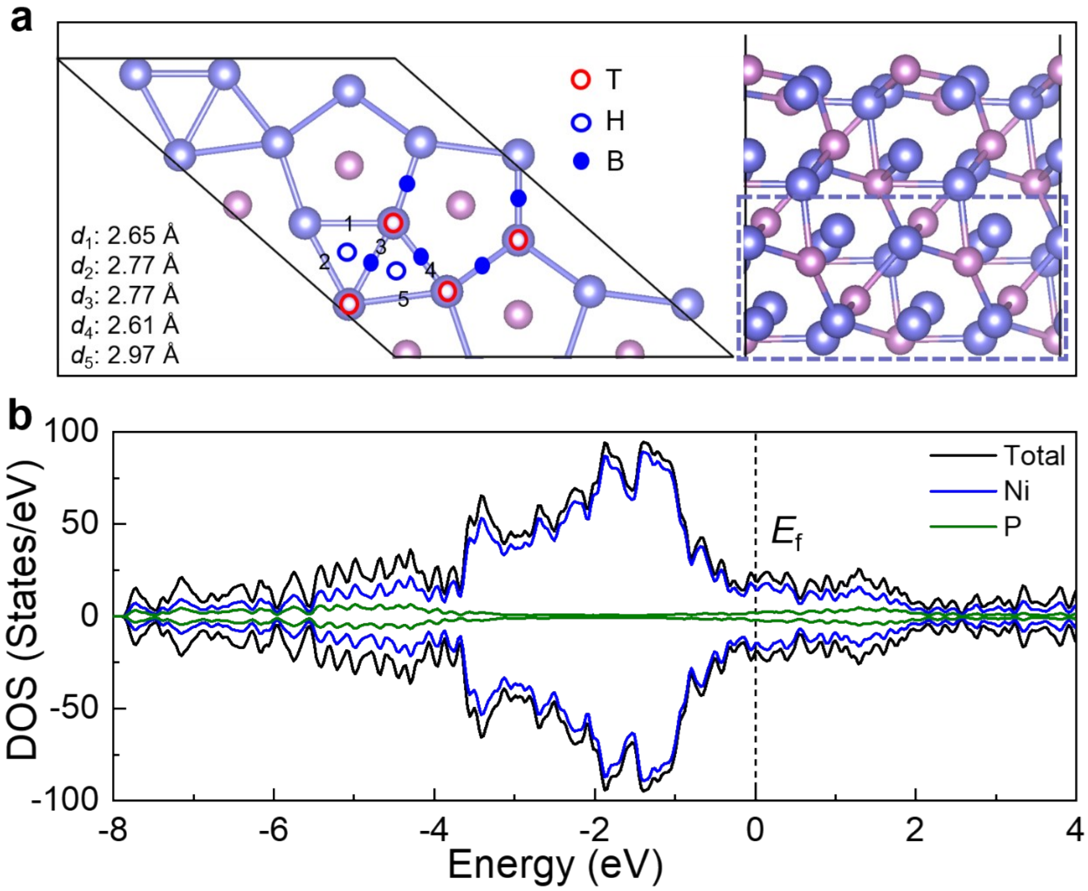

Fig. S29. (a) Top and side views of the Ni_2P (111) (1×2) supercell (the one with the lowest surface energy as shown in Fig. S22a). The adsorption sites for NO are marked. Several Ni-Ni bond lengths are displayed for comparison. (b) Total densities of states of the Ni_2P (111) (2×1) supercell and the local densities of states of the Ni and P atoms. The dashed line in (b) denotes the position of the Fermi level (E_f).

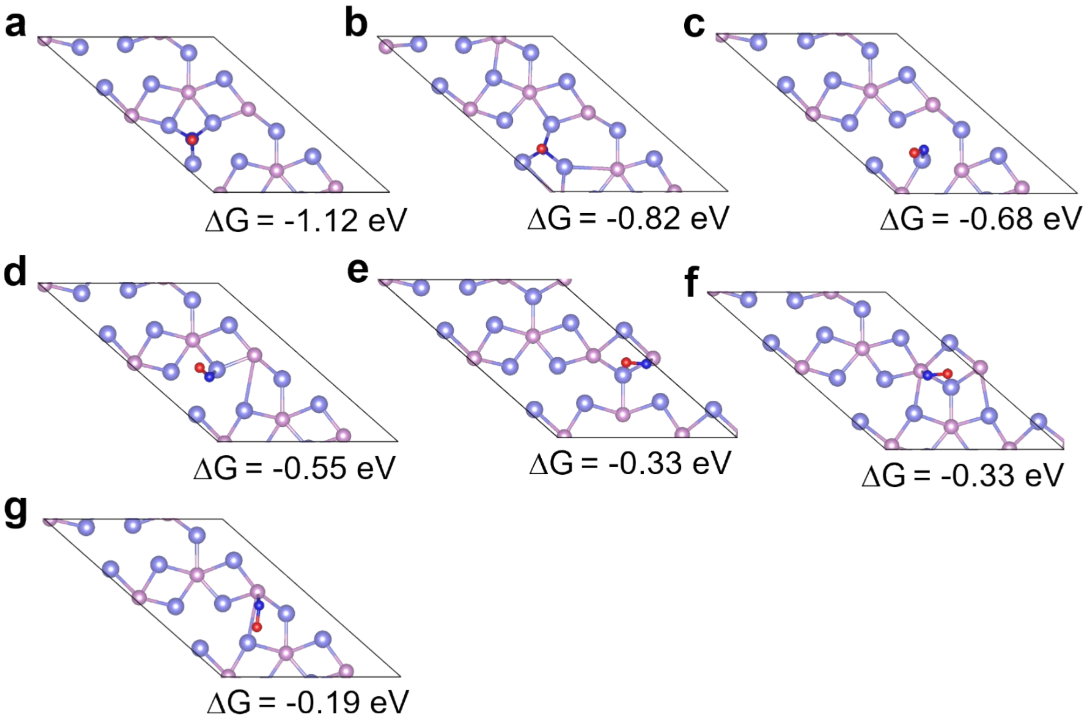

Fig. S30. Atomic structures together with the binding free energies are given for NO adsorption on the Ni_2P (111) (1×2) surface. Light blue, pink, dark blue, and red spheres represent Ni, P, N, and O atoms, respectively.

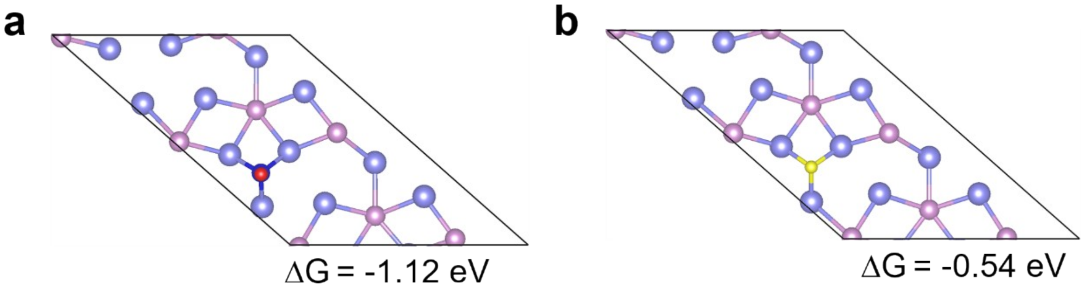

Fig. S31 Atomic structures together with the binding free energies of the most stable NO adsorption configuration and for the atomic H adsorption at the same site.

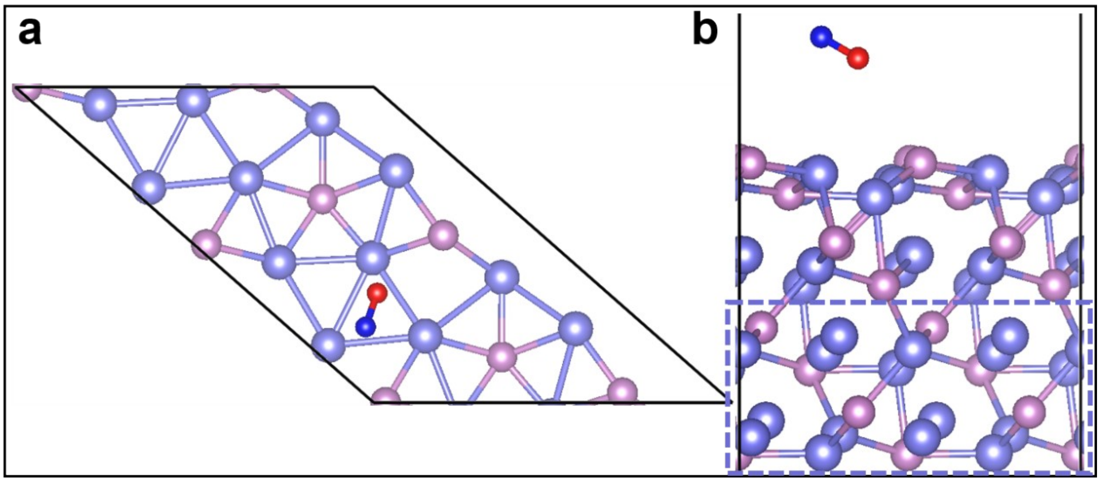

Fig. S32 Top (a) and side (b) views for NO adsorption with the O atom pointing toward the Ni_2P (111) (1×2) surface. Light blue, pink, dark blue, and red spheres represent Ni, P, N, and O atoms, respectively.

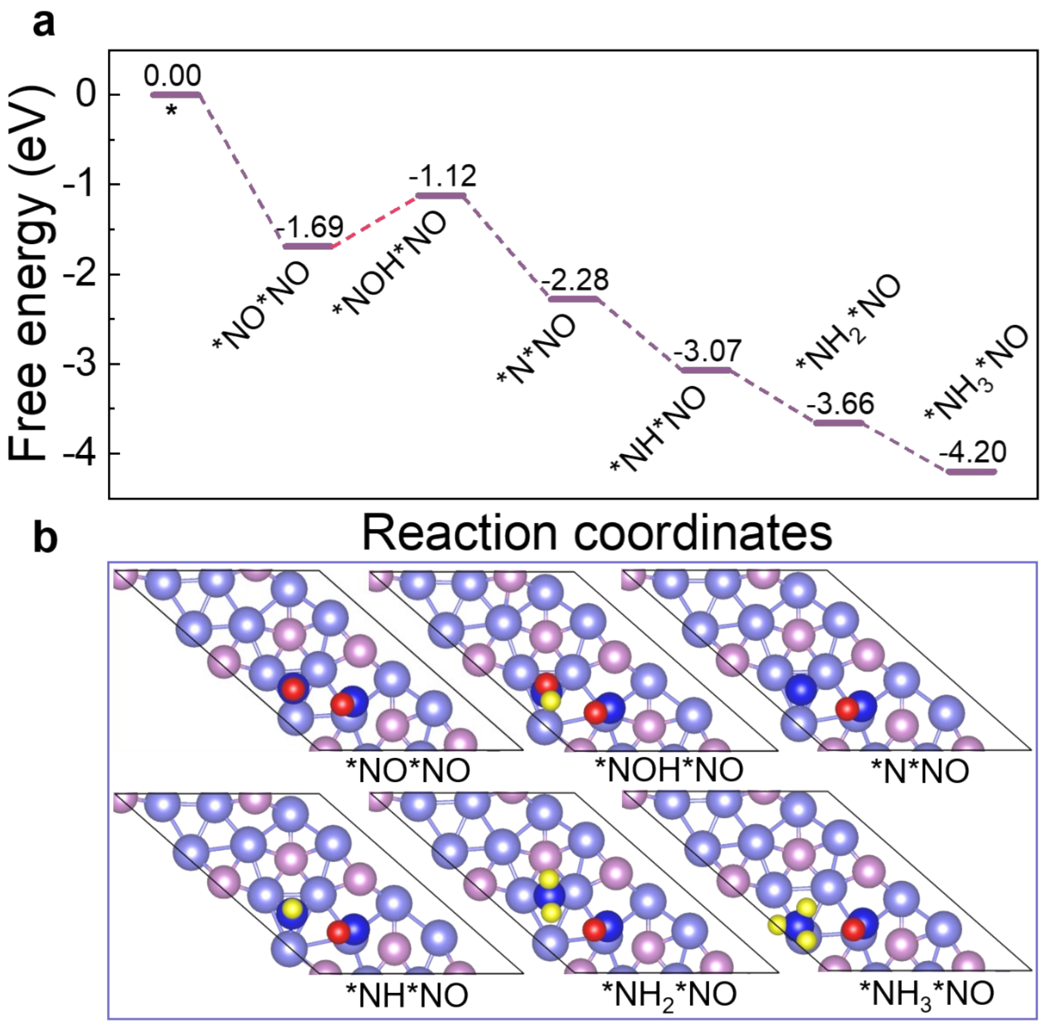

Fig. S33 (a) Free energy diagrams for the reduction of NO dimer on the Ni_2P (111) surface and (b) the atomic structures of the reaction intermediates along the pathways shown in (a). In (b), only the topmost atomic layer of the Ni_2P (111) surface and the adsorbed intermediates are displayed for clarity. Light blue, pink, dark blue, red, and yellow spheres represent Ni, P, N, O, and H atoms, respectively.

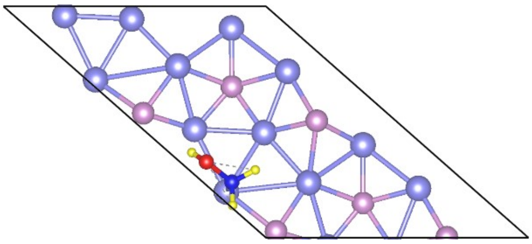

Fig. S34 Atomic configuration for the NH_2OH^*. Light blue, pink, dark blue, red, and yellow spheres represent Ni, P, N, O, and H atoms, respectively.

Table S1. Comparison of NH_3 yield and FE of Ni_2P/CP with reported aqueous-based NRR electrocatalysts.

Catalyst	Electrolyte	NH_3 yield	FE (%)	Ref.
Ni_2P/CP	**0.1 M HCl**	**9.3×10^{-9} mol s^{-1} cm^{-2}**	**76.9**	**This work**
Zr-doped α-FeOOH	0.1 M Na_2SO_4	0.139×10^{-9} mol s^{-1} cm^{-2}	35.63	*Appl. Surf. Sci.*, 2021, 150801
$FeNi_2S_4$/NiS	0.1 M KOH	2.1×10^{-9} mol s^{-1} cm^{-2}	28.6	*Appl. Catal. B*, 2021, **287**, 119956
Pd icosahedron	0.1 M Li_2SO_4	0.28×10^{-9} mol s^{-1} cm^{-2}	31.98	*J. Mater. Chem. A*, 2021, **9**, 13483−13489
S-B/CNFs	0.5 M K_2SO_4	0.06×10^{-9} mol s^{-1} cm^{-2}	22.4	*Appl. Catal. B*, 2021, **292**, 120144
Sb_2Te_3	0.1 M KOH	0.23×10^{-9} mol s^{-1} cm^{-2}	27.7	*Cell Rep. Phys. Sci.*, 2020, **1**, 100232
Fe-MoS_2	0.1 M KCl	1.6×10^{-9} mol s^{-1} cm^{-2}	31.6	*Chem*, 2020, **6**, 885–901
Y_1/NC	0.1 M HCl	0.35×10^{-9} mol s^{-1} cm^{-2}	12.1	*ACS Nano*, 2020, **14**, 1093−1101
CoVP@NiFeV-LDHs HHNTs	0.05 M H_2SO_4	0.44×10^{-9} mol s^{-1} cm^{-2}	13.8	*Appl. Catal. B*, 2020, **265**, 118559
pAu/NF	0.1 M Na_2SO_4	0.15×10^{-9} mol s^{-1} cm^{-2}	13.4	*Small*, 2019, **15**, 1804769
C@CoS@TiO_2	0.1 M Na_2SO_4	0.8×10^{-9} mol s^{-1} cm^{-2}	28.6	*Angew. Chem. Int. Ed.*, 2019, **131**, 19079–19083
Fe_3Mo_3C/C	1 M KOH	0.2×10^{-9} mol s^{-1} cm^{-2}	14.74	*Angew. Chem. Int. Ed.*, 2019, **58**, 15541–15547
NPG@ZIF-8	0.1 M Na_2SO_4	0.4×10^{-9} mol s^{-1} cm^{-2}	44	*Angew. Chem. Int. Ed.*, 2019, **58**, 15362–15366
CuO/RGO	0.1 M Na_2SO_4	0.18×10^{-9} mol s^{-1} cm^{-2}	3.9	*ChemCatChem*, 2019, **11**, 1441–1447
d-TiO_2	0.1 M HCl	0.124×10^{-9} mol s^{-1} cm^{-2}	9.17	*Nanoscale*, 2019, **11**, 1555–1562
Ag nanosheet	0.1 M HCl	0.046×10^{-9} mol s^{-1} cm^{-2}	4.8	*Chem. Commun.*, 2018, **54**, 11427–11430
Fe_3O_4	0.1 M Na_2SO_4	0.056×10^{-9} mol s^{-1} cm^{-2}	2.6	*Nanoscale*, 2018, **10**, 14386–14389
VN	0.1 M HCl	0.084×10^{-9} mol s^{-1} cm^{-2}	2.25	*ACS Sustainable Chem. Eng.*, 2018, **6**, 9545–9549
MoO_3	0.1 M HCl	0.48×10^{-9} mol s^{-1} cm^{-2}	1.9	*J. Mater. Chem. A*, 2018, **6**, 12974–12977
MoS_2	0.1 M Na_2SO_4	0.081×10^{-9} mol s^{-1} cm^{-2}	1.17	*Adv. Mater.*, 2018, **30**, 1800191

Table S2. Comparison of onset potential, NH_3 yield, and FE of Ni_2P/CP with reported aqueous-based NORR electrocatalysts.

Catalyst	Electrolyte	Purity of NO inlet gas	Feeding rate	Testing cell system	Onset potential	NH_3 yield	FE (%)	Ref.
Ni_2P/CP	**0.1 M HCl**	**10 *vol.*% NO**	**30 sccm**	**H–type cell**	**0 vs. RHE**	**9.3×10^{-9} mol s^{-1} cm^{-2}**	**76.9**	**This work**
FeNC (NORR)	0.1 M $HClO_4$	10 *vol.*% NO	60 sccm	Three-electrode glass cell	0.7 vs. RHE	5.61×10^{-9} mol s^{-1} cm^{-2}	5.1	*Nat. Commun.*, 2021, **12**, 1856
$Ru_{0.05}Cu_{0.95}$ (NORR)	0.5 M Na_2SO_4	1/4 (n/n)	50 mL min^{-1}	H-type cell	−0.45 V vs. Ag/AgCl	4.9×10^{-9} mol s^{-1} cm^{-2}	64.9	*Sci. China. Chem.*, 2021, DOI: 10.1007/s11426-021-1073-5
Single atom Nb (NORR)	0.1 M HCl	/	20 sccm	Three-channel flow cell	−0.1 V vs. RHE	82×10^{-9} mol s^{-1} cm^{-2}	77	*Nano Energy*, 2020, **78**, 105321
Cu foam (NORR)	0.25 M Li_2SO_4	/	30 mL min^{-1}	H-type cell	/	143×10^{-9} mol s^{-1} cm^{-2}	93.5	*Angew. Chem. Int. Ed.*, 2020, **59**, 9711–9718
Cu foil (NORR)	0.25 M Li_2SO_4	/	30 mL min^{-1}	H-type cell	0.45 V vs. RHE	26×10^{-9} mol s^{-1} cm^{-2}	/	
Pt foil (NORR)	0.25 M Li_2SO_4	/	30 mL min^{-1}	H-type cell	0.45 V vs. RHE	28×10^{-9} mol s^{-1} cm^{-2}	/	
$CoSe_2$@CNTs (NORR)	Na_2SO_4 + Fe(II)EDTA	/	30 mL min^{-1}	H-type cell	/	/	48.14	*Environ. Sci. Pollut. Res.*, 2017, **24**, 14249–14258

Table S3. Comparison of NH_3 yield and power density of our battery with recent metal–N_2 battery systems.

Catalyst	**NH_3 yield**	**Power density**	**Ref.**
Ni_2P/CP	**62.05 $\mu g\ h^{-1}\ mg^{-1}_{cat.}$ (43.44 $\mu g\ h^{-1}\ cm^{-2}$)**	**1.53 $mW\ cm^{-2}$**	**This work**
Fe 1.0 HTNs	0.172 $\mu g\ h^{-1}\ cm^{-2}$	0.02765 $mW\ cm^{-2}$	*J. Mater. Chem. A*, 2021, **9**, 4026−4035
CoPi/HSNPC	11.62 $\mu g\ h^{-1}\ mg^{-1}_{cat.}$	0.31 $mW\ cm^{-2}$	*J. Mater. Chem. A*, 2021, **9**, 11370−11380
VN@NSC-900	0.172 $\mu g\ h^{-1}\ cm^{-2}$	0.01642 $mW\ cm^{-2}$	*Appl. Catal. B: Environ.*, 2021, **280**, 119434
CoPi/NPCS	14.7 $\mu g\ h^{-1}\ mg^{-1}_{cat.}$	0.49 $mW\ cm^{-2}$	*ACS Appl. Mater. Interfaces*, 2021, **13**, 12106−12117
NbS_2	/	0.31 $mW\ cm^{-2}$	*Appl. Catal. B: Environ.*, 2020, **270**, 118892
Graphene/Pd	27.1 $mg\ h^{-1}\ g^{-1}_{cat.}$	/	*Energy Environ. Sci.*, 2020, **13**, 2888−2895
BNFC-800	/	127 $mW\ cm^{-2}$	*J. Mater. Chem. A*, 2020, **8**, 8430−8439
Cu-2	0.125 $\mu g\ h^{-1}\ cm^{-2}$	0.0101 $mW\ cm^{-2}$	*Chem. Commun.*, 2019, **55**, 12801−12804

Table S4. Theoretical voltages for different types of metal–based batteries.

Battery type	**Chemical reaction**	**Theoretical voltage (V)**
Zn–NO	$5Zn + 2NO + 3H_2O \rightarrow 5ZnO + 2NH_3$	2.14
Li–S	$2Li + S \rightarrow Li_2S$	2.2
Li–O_2	$2Li + O_2 \rightarrow Li_2O_2$	3.0
Li–CO_2	$4Li + 3CO_2 \rightarrow C + 2Li_2CO_3$	2.7
Li–N_2	$6Li + N_2 \rightarrow 2Li_3N$	0.54
Zn–CO_2	$Zn + CO_2 + H_2O \rightarrow ZnO + HCOOH$	0.955
Al–N_2	$2Al + N_2 \rightarrow 2AlN$	0.99
Zn–Air	$2Zn + O_2 \rightarrow 2ZnO$	1.65
Zn–Nitrate	$4Zn + NO_3^{-} + 3H_2O \rightarrow 4ZnO + NH_4OH + OH^{-}$	1.85

Table S5. Calculations of power density of the half-cell tests.

I (mA)	**U (V)**	**P (mW cm^{-2})**
2.68	0.57	1.53

Table S6. The calculated zero-point energy (E_{ZPE}) and the product (TS) of temperature (T = 298.15 K) and entropy (S) of the different species along the reaction pathway presented in Fig. 4(c), where * represents the adsorption site.

Species	E_{ZPE} (eV)	TS (eV)
*NO	0.18	0.13
*NOH	0.48	0.12
*N	0.08	0.03
*NHOH	0.79	0.16
*NH	0.39	0.04
$^*NH_2$	0.70	0.08
$^*NH_3$	1.03	0.15
H	0.14	0.20
NO	0.12	0.65
NH_3	0.89	0.60
H_2O	0.56	0.67
*NO*NO	0.35	0.22
*NO*NOH	0.65	0.29
*N*NO	0.26	0.20
*NH*NO	0.55	0.15
$^*NH_2{}^*NO$	0.88	0.17
$^*NH_3{}^*NO$	1.20	0.23

References

1 D. Zhu, L. Zhang, R. E. Ruther and R. J. Hamers, *Nat. Mater.*, 2013, **12**, 836−841.

2 G. W. Watt and J. D. Chrisp, *Anal. Chem.*, 1952, **24**, 2006−2008.

3 G. Kresse and J. Furthmüller, *Phys. Rev. B*, 1996, **54**, 11169.

4 J. P. Perdew, K. Burke and M. Ernzerhof, *Phys. Rev. Lett.*, 1996, **77**, 3865−3868.

5 P. E. Blöchl, *Phys. Rev. B*, 1994, **50**, 17953−17979.

6 S. Grimme, J. Antony, S. Ehrlich and H. Krieg, *J. Chem. Phys.*, 2010, **132**, 154104.

7 H. J. Monkhorst and J. D. Pack, *Phys. Rev. B*, 1976, **13**, 5188−5192.

8 G. Henkelman, A. Arnaldsson and H. Jónsson, *Comput. Mater. Sci.*, 2006, **36**, 354−360.

9 J. K. Nørskov, J. Rossmeisl, A. Logadottir, L. Lindqvist, J. R. Kitchin, T. Bligaard and H. Jónsson, *J. Phys. Chem. B*, 2004, **108**, 17886−17892.

10 http://webbook.nist.gov/chemistry/